The Seasonal Effects of ENSO on Atmospheric Conditions Associated with European Precipitation: Model Simulations of Seasonal Teleconnections

JEFFREY SHAMAN

Department of Environmental Health Sciences, Columbia University, New York, New York

(Manuscript received 17 October 2012, in final form 1 September 2013)

ABSTRACT

The seasonal upper-tropospheric teleconnection between ENSO and the North Atlantic/European sector is explored through a series of model experiments. A barotropic vorticity equation model is linearized about climatological conditions for each season of the year, and divergence forcing is applied over the equatorial Pacific to mimic El Niño–related convective activity. During boreal fall, winter, and spring, this forcing similarly excites a northeastward-propagating stationary barotropic Rossby wave train that extends across the North Atlantic to the European coast. Strong anomalies develop over the British Isles in the vicinity of the North Atlantic jet exit. Solutions during boreal summer produce no clear wave train; however, evidence exists for a North Atlantic response because of both eastward- and westward-propagating signals. These direct responses over the Atlantic and Europe are qualitatively similar to observed ENSO-associated anomalies during boreal spring and fall, but differ structurally during summer and winter. Further experiments with the vorticity equation model using full Rossby wave source forcing, which included vorticity advection, increase the amplitude of the response over Europe during some seasons; however, structural differences persist.

Finally, experiments with the Community Atmosphere Model (CAM), version 4, reveal that the basic northeastward-propagating response is modulated by downstream feedbacks. These changes are most profound during boreal winter and engender an arching wave train pattern that, matching observations, reflects off the jet over North America, propagates southeastward over the North Atlantic, and fails to reach the European coast. Overall, the simulations with CAM correctly depict observed seasonal changes in the magnitude of the ENSO–North Atlantic/European teleconnection by producing a strong fall and winter response but a weaker spring and summer response. The CAM experiments also indicate that the seasonal response is not dependent on antecedent conditions; however, CAM simulations fail to project the upper-tropospheric anomalies appropriately to the lower troposphere.

1. Introduction

This work builds on analysis that used observations to explore the seasonal relationship between the El Niño–Southern Oscillation (ENSO) and European precipitation (Shaman 2013, manuscript submitted to *J. Climate*). Previous work has suggested that at least some of these seasonal teleconnections may be mediated by anomalous upper-tropospheric Rossby wave activity forced by ENSO-related changes to precipitation rates over the equatorial Pacific (Park 2004; Shaman and Tziperman 2011); however, how this teleconnection varies through the calendar year and whether its role linking the equatorial Pacific and North Atlantic/European sectors is important in all seasons remains undetermined.

Some prior modeling studies have explored the teleconnection between ENSO and the North Atlantic, particularly during boreal winter. Model simulations are often consistent with observations over the North Atlantic (Dong et al. 2000; Greatbatch et al. 2004; Greatbatch and Jung 2007); however, the response over Europe is much less robust and less explored. For instance, model simulations with the ECHAM4 AGCM have been able to replicate many observed winter and summer ENSO teleconnections around the planet; however, teleconnections between ENSO and Europe are not consistently well resolved (Grötzner et al. 2000). Subsequent work with the ECHAM4 model showed that the response of the North Atlantic/European sector to ENSO was sensitive to model resolution and that at a higher resolution a better Northern Hemisphere wintertime response was simulated (Merkel and Latif 2002).

Corresponding author address: Jeffrey Shaman, Department of Environmental Health Sciences, Mailman School of Public Health, Columbia University, 722 West 168th Street, Rosenfield Building, Room 1104C, New York, NY 10032.
E-mail: jls106@columbia.edu

DOI: 10.1175/JCLI-D-12-00734.1

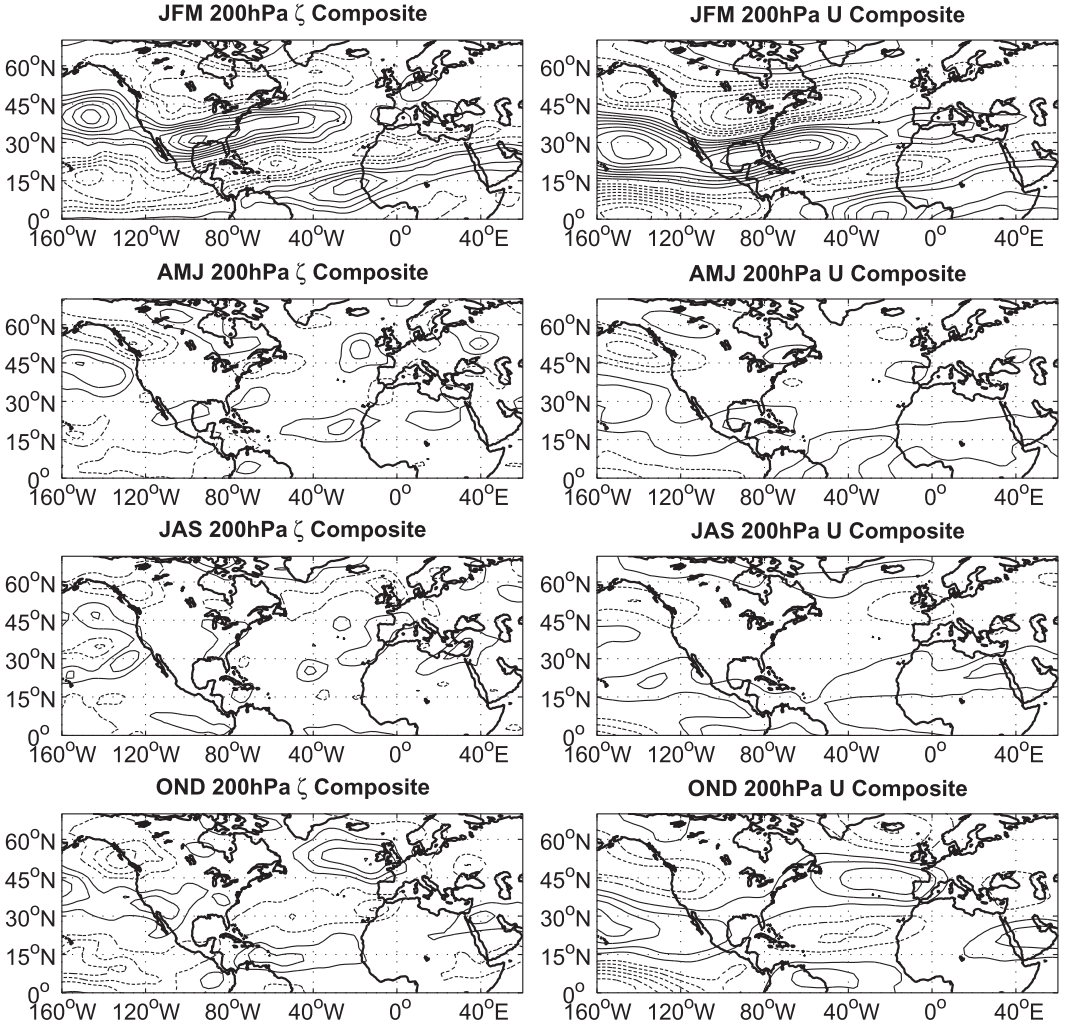

FIG. 1. The 3-month seasonal ENSO-based composites of NNR 200-hPa (left) relative vorticity and (right) zonal wind made using Niño-3.0 SSTs. The contour intervals are (left) $4 \times 10^{-6}\,s^{-1}$ and (right) $2\,m\,s^{-1}$. Negative contours are dotted and the zero contour is omitted.

Feddersen (2003) decomposed Météo-France AGCM simulations and found some skill in the representation of spring precipitation over Scandinavia. The upper-tropospheric barotropic response to ENSO along the west coast of Europe for boreal fall has been represented with a simple linearized model (Shaman and Tziperman 2011), and this pattern is associated with anomalous onshore moisture to southern Europe.

Here, seasonal teleconnections between ENSO and upper-tropospheric variability over the North Atlantic and Europe are further explored using a hierarchy of models. Model simulations of individual ENSO events with different SST anomaly patterns can yield different responses in the North Atlantic/European sector (Mathieu et al. 2004); however, in this study the focus will be the average upper-tropospheric response to ENSO rather than individual events. Instantaneous, within season teleconnections mediated by rapidly propagating atmospheric Rossby wave teleconnections will be the principal focus. Model simulations will be compared primarily to seasonal ENSO-associated upper-tropospheric anomalies over the North Atlantic and Europe, as presented in Shaman (2013, manuscript submitted to *J. Climate*) and reproduced again here for clearer comparison (Fig. 1).

The remainder of the paper is organized as follows. Section 2 describes the models and methods used in this study. Section 3 presents the results from simulations with a barotropic vorticity equation model linearized about climatological reanalysis fields for all four seasons: January–March (JFM), April–June (AMJ), July–September (JAS), and October–December (OND). Simulations with an atmospheric general circulation model

(AGCM) are then presented in section 4. Climatological fields derived from the AGCM simulations are then used as the basis for further experiments with the linearized barotropic vorticity equation model (section 5). Section 6 presents discussion.

2. Methods

Simulations were performed with both a linearized barotropic vorticity equation (LBVE) model and an AGCM. For the LBVE model, the barotropic vorticity equation was first linearized about a low-pass filtered (zonal wavenumbers 0–8) background streamfunction field, for example, JFM 1949–2011 National Centers for Environmental Prediction–National Center for Atmospheric Research (NCEP–NCAR) reanalysis (NNR) 200-hPa streamfunction (Kalnay et al. 1996). Two forms of the LBVE model were utilized. In the first form, steady forced solutions of the LBVE were found following the solution method of Branstator (1983):

$$J(\overline{\psi}, \nabla^2\psi') + J(\psi', \nabla^2\overline{\psi} + f) + \nu\nabla^2\psi' + \kappa\nabla^4\nabla^2\psi' = R, \tag{2.1}$$

where ψ is streamfunction, f is the Coriolis force, ν is the Rayleigh coefficient, κ is a diffusion coefficient, and R is a forcing function;

$$J(A, B) = \frac{1}{r^2}\left(\frac{\partial A}{\partial\lambda}\frac{\partial B}{\partial\mu} - \frac{\partial A}{\partial\mu}\frac{\partial B}{\partial\lambda}\right)$$

is the Jacobian, r is the Earths radius, λ is longitude, and $\mu = \sin(\varphi)$, where φ is latitude. Here, the overbars indicate the seasonal time-mean flow (the basic state) and primes signify the perturbation flow to be solved. The coefficient ν was set to $1.57 \times 10^{-6}\,\mathrm{s}^{-1}$ (an e-folding time of $1/7\,\mathrm{day}^{-1}$), and κ was set to $2.34 \times 10^{16}\,\mathrm{m}^4\,\mathrm{s}^{-1}$. The anomaly forcing was specified as $R = -(f + \nabla^2\overline{\psi})D'$, where D', the perturbation forcing divergence, was set to $3 \times 10^{-6}\,\mathrm{s}^{-1}$ for all experiments and was spatially restricted to the area of perturbation. Equation (2.1) was solved using spherical harmonics and with a triangular 24 truncation (T24).

The second LBVE form was integrated with full Rossby wave source forcing, as in Sardeshmukh and Hoskins (1988):

$$\frac{\partial\zeta}{\partial t} + J(\overline{\psi}, \nabla^2\psi') + J(\psi', \nabla^2\overline{\psi} + f) + \nu\nabla^2\psi' + \kappa\nabla^4\nabla^2\psi' = R_f, \tag{2.2}$$

where

$$R_f = -\nabla\cdot[\nabla\chi'(\nabla^2\overline{\psi} + f)] - \nabla\cdot(\nabla\overline{\chi}\nabla^2\psi') \tag{2.3}$$

is the full Rossby wave source, representing not only divergence forcing (i.e., vortex stretching), but also vorticity advection by the divergent wind, and χ is the velocity potential (e.g., JFM 1949–2011 NNR 200-hPa velocity potential). As for the steady-state solution, divergence ($\nabla^2\chi' = D'$) was set to a constant $3 \times 10^{-6}\,\mathrm{s}^{-1}$ in the forcing region. Per Sardeshmukh and Hoskins (1988), uniform compensating convergence was applied elsewhere globally. Solutions were found by integrating Eq. (2.2) forward in time for 50 days.

Simulations were also performed using the Community Atmosphere Model (CAM), version 4 (CAM4; Neale et al. 2010), an AGCM forced with merged Hadley Centre optimal interpolation (OI) SSTs and sea ice concentrations (Hurrell et al. 2008). CAM simulations were run at 1.9° × 2.5° resolution with 26 levels in the vertical.

Two types of experiments were performed with the AGCM. The first involved running a long CAM simulation with SST forcing from 1868 through 2009. The output from this simulation was used to generate El Niño minus La Niña composites of various atmospheric fields. Only the period from 1870 to 1999 was included in these composites. Specifically, a seasonal index of monthly SST anomalies for the Niño-3.0 region (5°S–5°N, 150°–90°W) was constructed from the Hadley Centre OI SST forcing set. Years for which the index was in excess of plus or minus one standard deviation were then identified. For a given field (e.g., 200-hPa relative vorticity), seasonal composites were then constructed by subtracting conditions for that season averaged for all negative phase (e.g., La Niña) years from conditions for that season averaged for all positive phase (El Niño) years.

For the second suite of experiments, CAM was run with a perpetual setting of either 14 February, 15 May, 15 August, or 15 November. In this setting, orbital forcing was fixed to one of these specified dates; however, the model diurnal cycle was retained. Each perpetual setting of the model was then integrated for 20 yr with average monthly El Niño or La Niña SST forcing for the entire planet or only in the equatorial Pacific (30°S–30°N) and climatological monthly SSTs everywhere else. The average monthly El Niño and La Niña boundary conditions were derived from the Hadley Centre OI SST and sea ice forcing set. El Niño minus La Niña composites of various atmospheric fields were then constructed from years 11–20 of these runs.

Some additional analyses of precipitation were performed using three different gridded monthly datasets:

1) the 1979–2010 National Oceanic and Atmospheric Administration (NOAA) NCEP Climate Anomaly Monitoring System (CAMS)–outgoing longwave radiation precipitation index (OPI) (CAMS–OPI; Janowiak and Xie 1999); 2) the 1979–2008 National Aeronautics and Space Administration (NASA) Global Precipitation Climatology Project (GPCP), version 2.1 (Adler et al. 2003); and 3) the 1979–2010 NOAA NCEP Climate Prediction Center (CPC) Merged Analysis of Precipitation (CMAP; Xie and Arkin 1997). All three precipitation datasets are gridded at 2.5° × 2.5° resolution. The CAMS–OPI and NASA GPCP precipitation are both derived from satellite and gauge estimates. The CMAP precipitation is a merging of satellite estimates, gauge estimates, and numerical predictions.

3. LBVE model results

Seasonal ENSO-based composites of precipitation over the tropical Pacific were generated using the CAMS–OPI precipitation dataset (Fig. 2). These composites were used to guide the application of divergence forcing for the LBVE model. All four seasons show that ENSO rainfall anomalies manifest over the Pacific Ocean along the intertropical convergence zone (ITCZ) north of the equator. During winter, the anomalies are most concentrated around the date line, and the weakest rains are in the spring. However, for the coarse forcing used with the LBVE model, there is little appreciable difference of ENSO-related precipitation anomalies among the seasons. Along the ITCZ, where much of the precipitation occurs, the intensity of the precipitation anomalies varies by at most a factor of 2. Seasonal ENSO-based composites made with the GPCP and CMAP precipitation datasets produced similar results.

The anomalous mass transport and upper-tropospheric heating produced by altered convective activity creates localized horizontal divergence in the upper troposphere. Using the ENSO-based precipitation composites as a guide, experiments were performed principally with one of two expanses of divergence forcing imposed on the LBVE model. The first represents El Niño–related Northern Hemispheric forcing as a result of convection along the ITCZ and spanned 0°–10°N, 170°E–90°W. The second includes regions farther west as well as to the south of the equator in the South Pacific convergence zone (SPCZ) and spanned 10°S–10°N, 150°E–150°W and 0°–10°N, 150°–90°W. These regions of divergence forcing represent the anomalous mass transport and upper-tropospheric heating imposed by the increased precipitation during El Niño events.

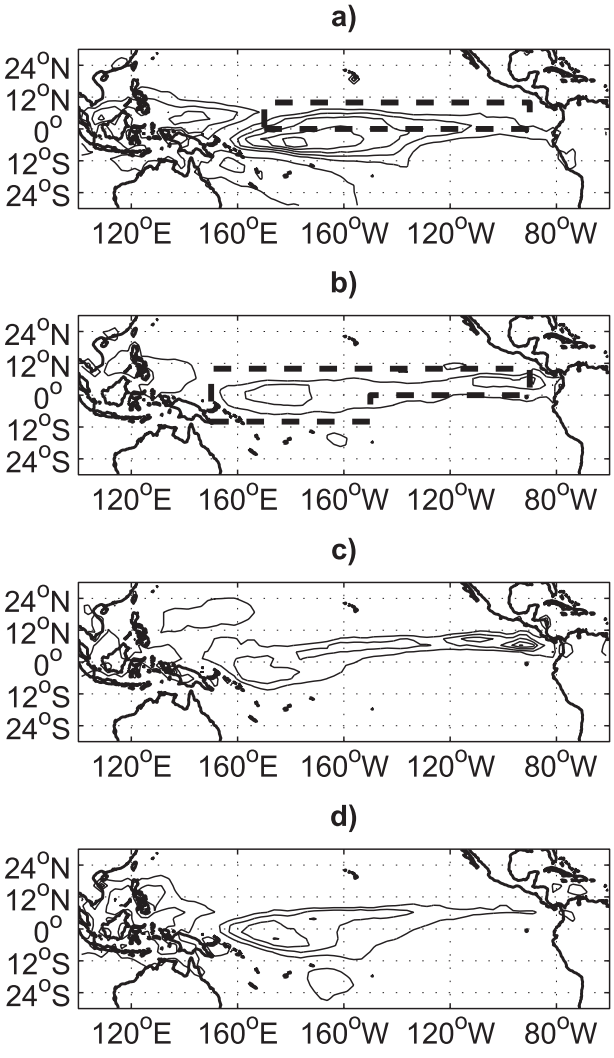

FIG. 2. The 3-month seasonal ENSO-based composites of CAMS–OPI precipitation made using Niño-3.0. Different seasons are presented in each panel: (a) JFM, (b) AMJ, (c) JAS, and (d) OND. The contour interval is 2.5 mm day^{-1} and the zero contour is omitted. Also shown in thick dashed lines are boxes outlining the principal regions where divergence forcing was imposed within the LBVE model: 0°–10°N, 170°E–90°W in (a) and 10°S–10°N, 150°E–150°W and 0°–10°N, 150°–90°W in (b).

a. Steady response to divergent forcing

Figure 3 presents the seasonal steady-state response of the LBVE model [Eq. (2.1)] to divergence applied in the first forcing region. For the JFM, AMJ, and OND seasons, the response is similar and characterized by a northeastward-propagating stationary barotropic Rossby wave train that produces a large positive vorticity anomaly over the North Atlantic. For the AMJ and OND seasons, these vorticity solutions are similar to the anomalies seen over the North Atlantic in seasonal NNR ENSO-based composites (Fig. 1). Indeed, for the AMJ season, the

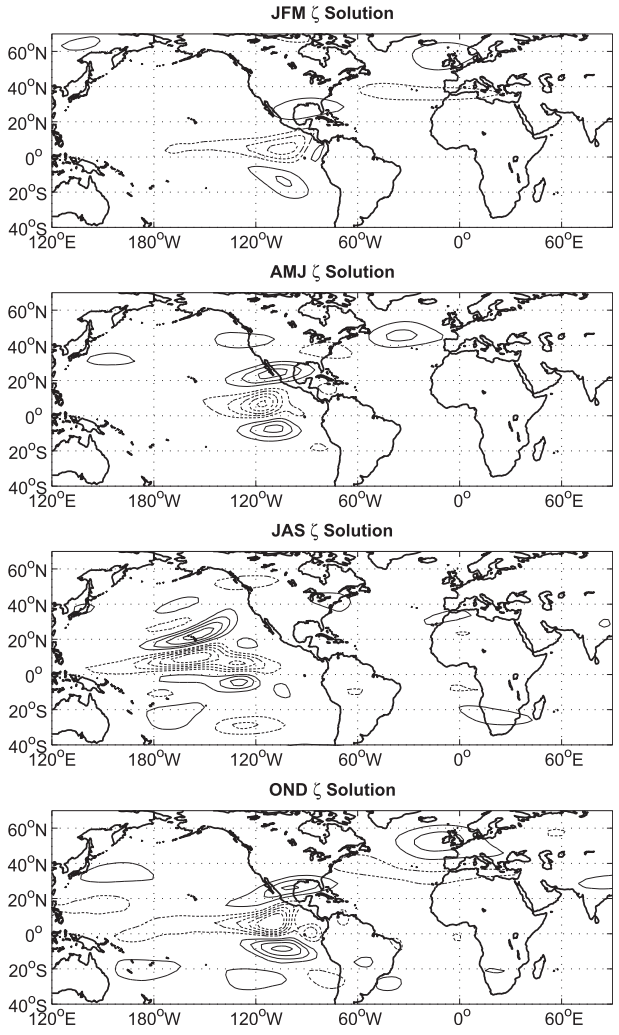

FIG. 3. Vorticity solution of steady-state LBVE model linearized about 3-month seasonal 200-hPa NNR background and forced with perturbation divergence from 0°–10°N, 170°E–90°W. The contour interval is $4 \times 10^{-6}\,s^{-1}$. Negative contours are dashed and the zero contour is omitted.

LBVE model captures more zonal orientation of the wave train with a negative vorticity anomaly over the eastern U.S. seaboard and a positive anomaly to the southwest of the British Isles. As expected, the AMJ NNR ENSO-based composite is noisier than the LBVE solution, which is only the direct linear barotropic response to the applied divergence forcing.

The OND LBVE solution is consistent with the response previously reported for the September–December (SOND) season (Shaman and Tziperman 2011). This solution captures the north–south dipole with nodes centered just to the west of the British Isles and North Africa. The positive node of the dipole is stronger during boreal fall than spring in both the model solution and NNR ENSO-based composites (Fig. 1). This positive node is at the end of the North Atlantic jet where eddy momentum fluxes are great and where tropical forcing is expected and previously has been shown to have a large direct effect on mean conditions (Hoerling and Ting 1994; Held et al. 2002).

For the JFM season the LBVE solution produces a dipole similar to that seen for the OND season, though slightly weaker and shifted to the north. This response is dissimilar to JFM NNR ENSO-based composites of 200-hPa vorticity. Specifically, the JFM LBVE solution is much weaker than the composites and appears to be much too far to the north and east. Indeed, the JFM NNR ENSO-based composite anomalies suggest a wave train that passes to the south and west of continental Europe over the western Atlantic Ocean before entering the North African–Asian (NAA) jet (see also Shaman and Tziperman 2005). Strong anomalies over the North Pacific are also evident in the JFM NNR ENSO-based composites. The LBVE solution fails to replicate these features.

For the JAS season, the LBVE solution over the North Atlantic is weak and confined to the NAA jet (visible over North Africa and the Straits of Gibraltar). This lack of response is somewhat consistent with the JAS NNR ENSO-based composite of relative vorticity, which shows a limited response over the North Atlantic and statistically significant anomalies in the NAA jet (Fig. 1).

The largest JAS LBVE response occurs over the Pacific Ocean and is centered within the longitudes of the forcing region (170°E–90°W). For the other three seasons the bulk of the response over the Pacific is shifted preferentially to the eastern portion of the forcing region. This difference may reflect changes in the upper-tropospheric winds. During JAS easterly winds prevail at 200 hPa between 0° and 10°N across the entire Pacific, whereas during the other seasons an expanse of westerlies appears over the central and eastern equatorial regions (Fig. 4). Indeed, during JAS the most equatorward westerlies over the North Pacific are associated with the subtropical jet centered at 20°N, 160°W. This region is coincident with a large positive vorticity response in the LBVE solution (Fig. 3).

The boreal summer equatorial easterlies appear to advect the vorticity response to the central Pacific, whereas during the other seasons the equatorial westerlies appear to shift the response to the eastern Pacific. In addition, it is only for the three seasons with westerlies in the forcing region that a canonical poleward and eastward stationary Rossby wave response is produced by the LBVE model. For a zonally symmetric background, westerlies are necessary to support stationary Rossby wave trains

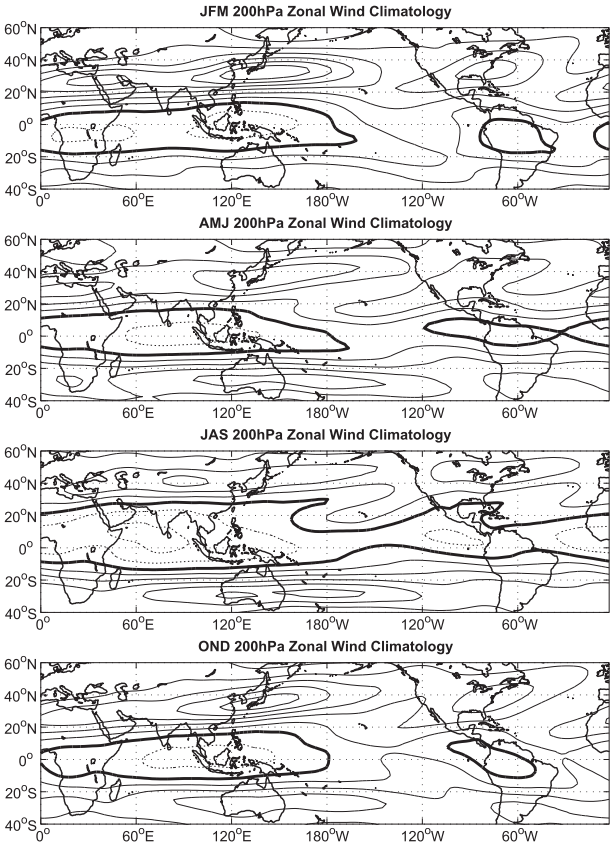

FIG. 4. The 3-month seasonal 1949–2011 NNR 200-hPa zonal wind climatologies. The contour interval is $10\,\mathrm{m\,s^{-1}}$. Negative contours are dashed and the zero contour is thickened.

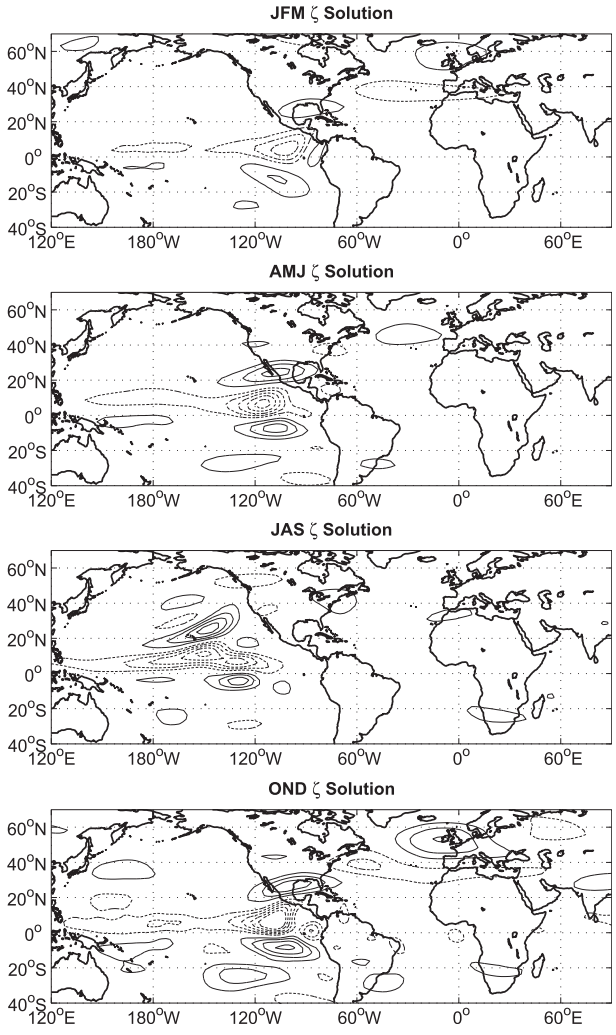

FIG. 5. As in Fig. 3, but with perturbation divergence forcing from 10°S–10°N, 150°E–150°W and 0°–10°N, 150°–90°W. The contour interval is $4 \times 10^{-6}\,\mathrm{s^{-1}}$. Negative contours are dashed and the zero contour is omitted.

(Hoskins and Karoly 1981). While westerlies are not required to support stationary Rossby waves in zonally varying backgrounds, such as are used here, there does seem to be an effect associated with the zonal wind direction with a clear poleward and eastward wave train during JFM, AMJ, and OND, but not during JAS.

Simulations with the steady-state LBVE model were next repeated using the second forcing region (10°S–10°N, 150°E–150°W and 0°–10°N, 150°–90°W). This more complete ENSO-related forcing does not affect the LBVE solutions much (Fig. 5). Indeed, the JFM and JAS responses are virtually unchanged from the first forcing (Fig. 3). Over the North Atlantic, the AMJ response weakens slightly and the OND response strengthens (Fig. 5). Both of these changes are more consistent with composite findings, which indicate a stronger ENSO-related change in upper-tropospheric vorticity during boreal fall than boreal spring (Fig. 1). The similarity in response to the two forcing regions indicates that the bulk of the North Atlantic and European response in the steady LBVE model is derived from ENSO-related divergence forcing over the eastern equatorial Pacific.

Next, seasonal simulations with the steady-state LBVE model and the first forcing region were repeated but with a sponge layer of high Rayleigh damping applied pole-to-pole and centered at 90°W (per Shaman and Tziperman 2007). Disturbances impinging upon this sponge layer are quickly damped out. The sponge layer is positioned to the east of the forcing region and thus greatly reduces eastward-propagating wave trains. The LBVE model solutions with this damping reveal almost no response over the North Atlantic and Europe, except during the JAS season (Fig. 6). These solutions indicate that during the JFM, AMJ, and OND seasons, the vorticity response over the North Atlantic and Europe, as represented by the LBVE model, derives from an eastward-propagating signal.

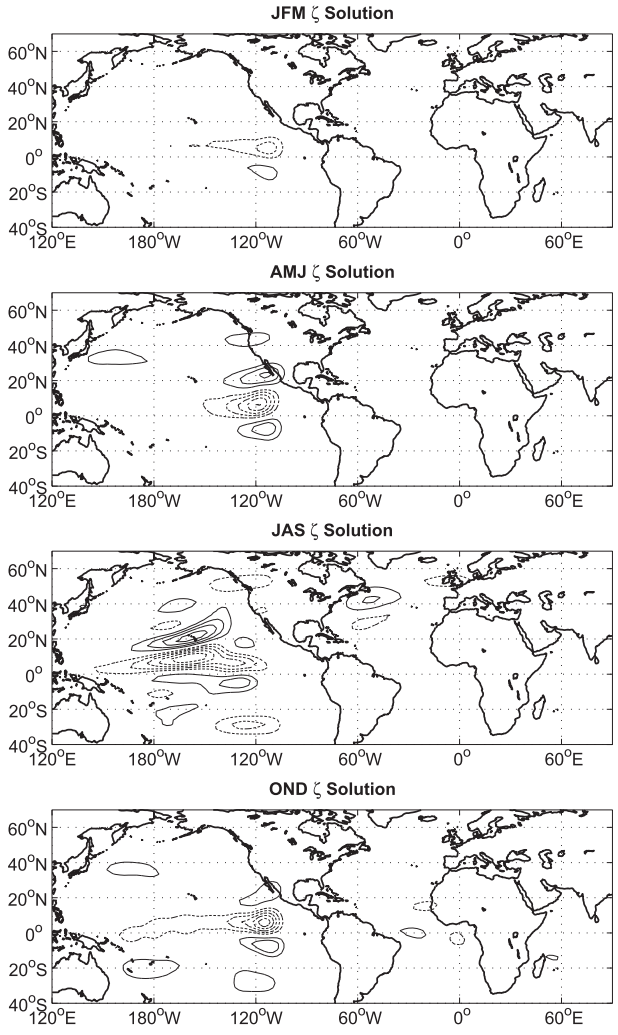

FIG. 6. As in Fig. 3, but with a pole-to-pole sponge layer of increased damping applied and centered at 90°W.

For the JAS season, the vorticity response over the North Atlantic intensifies with the damping of eastward-propagating signals. This change suggests that during this season both eastward- and westward-propagating signals exist and interfere with one another over the North Atlantic. Indeed, simulation of the LBVE model with the same forcing, but a sponge layer centered at 150°E, produces a large negative anomaly over the North Atlantic centered at 45°N, 30°W (Fig. 7). This vorticity response matches the weak feature seen over the North Atlantic in ENSO-based composites (Fig. 1). Thus, it appears that ENSO-related forcing of the LBVE model during the JAS season does produce an eastward-propagating signal, though without a clear wave train. The response over the North Atlantic is weak and canceled out by a westward-propagating signal.

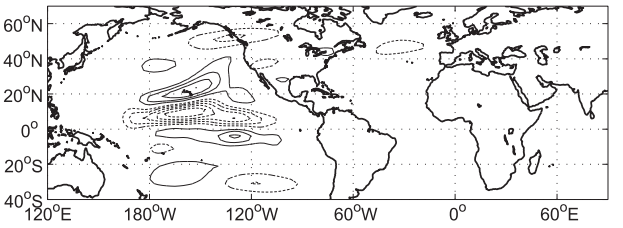

FIG. 7. As in Fig. 3, but only shown for the JAS season and with a pole-to-pole sponge layer of increased damping applied and centered at 150°E.

Overall, these steady-solution LBVE model results indicate that the upper-tropospheric response over the North Atlantic observed in ENSO-based composites for the OND and AMJ seasons is consistent with a simple linear barotropic response to El Niño–related divergence forcing over the equatorial Pacific. However, the LBVE model simulations with basic perturbation divergence forcing for the JFM season do not capture the features seen in composites for that season, suggesting that other processes are involved in producing the observed response. Indeed, this form of the LBVE model has a single response pattern over the North Atlantic for the JFM, AMJ, and OND seasons that consists of a northeastward-propagating wave train. This wave train seems to amplify in the vicinity of the British Isles, producing a stronger anomaly in this region, which is coincident with the exit of the North Atlantic jet. During JAS, some of the features seen in composites are reproduced by an eastward-propagating signal; however, this signal is weak and the Northern Hemisphere response to ENSO forcing is predominantly restricted to the Pacific basin and a westward-propagating signal in the NAA jet (as shown in Shaman and Tziperman 2007; Shaman et al. 2009).

b. Time-integrated Rossby wave source response

The time-integrated version of the LBVE model [Eq. (2.2)] was next used to explore the effects of full Rossby wave source ENSO-related forcing on upper-tropospheric conditions. The full Rossby wave source [Eq. (2.3)] includes linearized vortex stretching terms and vorticity advection by the divergent wind. With the inclusion of the additional forcing terms, the day 50 JFM response captures the pattern of alternately signed vorticity anomalies that propagate northeastward over the United States then recurve southeastward over the subtropical Atlantic (Fig. 8). This wave train matches the vorticity pattern seen in reanalysis composites (Fig. 1). As in the composites, this wave train pattern is centered over the western Atlantic away from Europe; however, unlike the NNR composites, a dipole of positive vorticity centered west

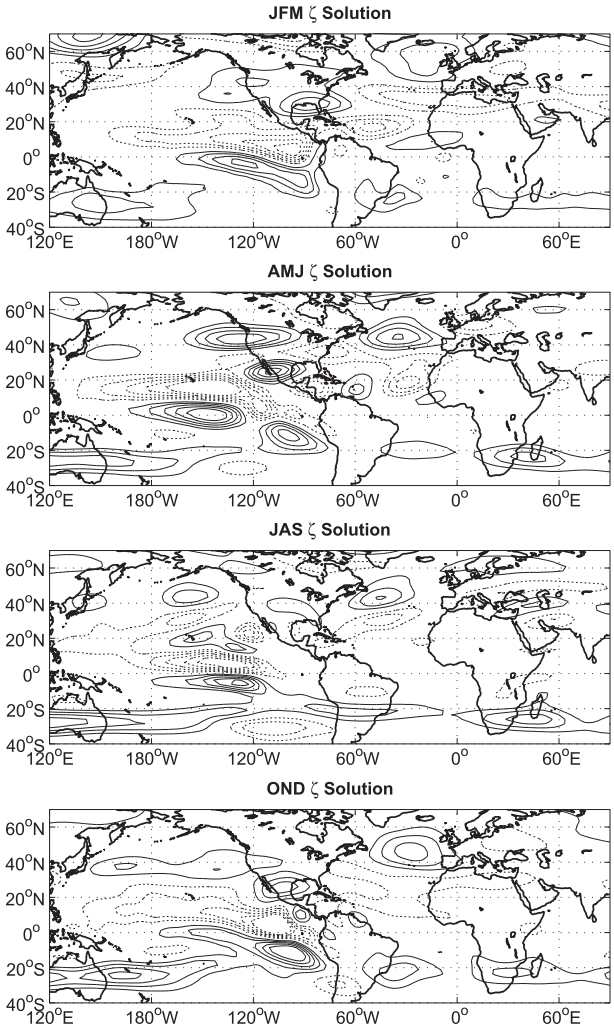

FIG. 8. Vorticity solution for day 50 of the time-integrated LBVE model linearized about 3-month seasonal 200-hPa NNR background and forced with full Rossby wave source forcing [Eq. (2.3)], including perturbation divergence from 0°–10°N, 170°E–90°W. The contour interval is $4 \times 10^{-6}\,s^{-1}$. Negative contours are dashed and the zero contour is omitted.

of the British Isles and negative vorticity to the south remains.

For the AMJ season, the day 50 LBVE model Atlantic basin response to full Rossby wave source forcing is dominated by a vorticity dipole. This response is much more pronounced than in either the steady-state response (Fig. 3) or the NNR composites. As for the steady-state simulation, the time-integrated full Rossby wave source–forced solution anomalies are farther west over the North Atlantic than the weak dipole anomalies seen in the NNR composites (Fig. 1). A negative vorticity anomaly over northern Europe is also seen in the time-integrated full Rossby wave source–forced solution (Fig. 8), which is also evident in the reanalysis composites.

For the JAS season, a vorticity dipole is produced over the western North Atlantic in the full Rossby wave source–forced LBVE model solution. A similar solution is produced in the steady-state LBVE model with damping applied at 90°W (Fig. 6). No corresponding dipole feature is evident in the JAS NNR composite.

The time-integrated response to full Rossby wave source forcing during the OND season (Fig. 8) is similar to the steady-state response to divergent forcing (Fig. 3). A vorticity dipole solution develops over the North Atlantic that corresponds to ENSO-derived NNR composite anomalies (Fig. 1; though this time-integrated model solution is shifted somewhat to the south and west).

A similar set of vorticity solutions is seen for all seasons in time-integrated solutions of the LBVE model with full Rossby wave source forcing and a sponge layer of damping centered at 150°E (not shown). This finding indicates that the ENSO-related response of this version of the LBVE model in the North Atlantic/European sector is primarily because of eastward-propagating signals.

Finally, the effect of the forcing location on the Rossby wave response was tested further by subdividing the forcing along the ITCZ. Figure 9 shows the seasonal solutions to full Rossby wave source forcing applied from 0°–10°N, 150°–90°W, and Fig. 10 shows the same for full Rossby wave source forcing applied from 0°–10°N, 150°E–150°W. These figures demonstrate that the upper-tropospheric vorticity response over North America and the North Atlantic is principally a result of forcing over the eastern equatorial Pacific. Indeed, further experiments reveal that the region east of 120°W is particularly critical for the excitation of these wave trains (not shown). A similar sensitivity to forcing location is also seen in steady solutions of the LBVE model.

Overall, the time integrations of the LBVE model with full Rossby wave source forcing indicate that additional source terms, including vorticity advection by the divergent wind, are needed to represent some of the features seen in reanalysis composites. In particular, the wave train structure observed over North America and the western North Atlantic during boreal winter is produced in this model setting with these additional terms.

4. CAM4 simulations

The seasonal teleconnection between ENSO and the North Atlantic/European sector was next explored using simulations with the CAM4. This model was used to provide a more complete representation of the atmospheric processes, most of which are not simulated by the LBVE model, that potentially mediate this teleconnection.

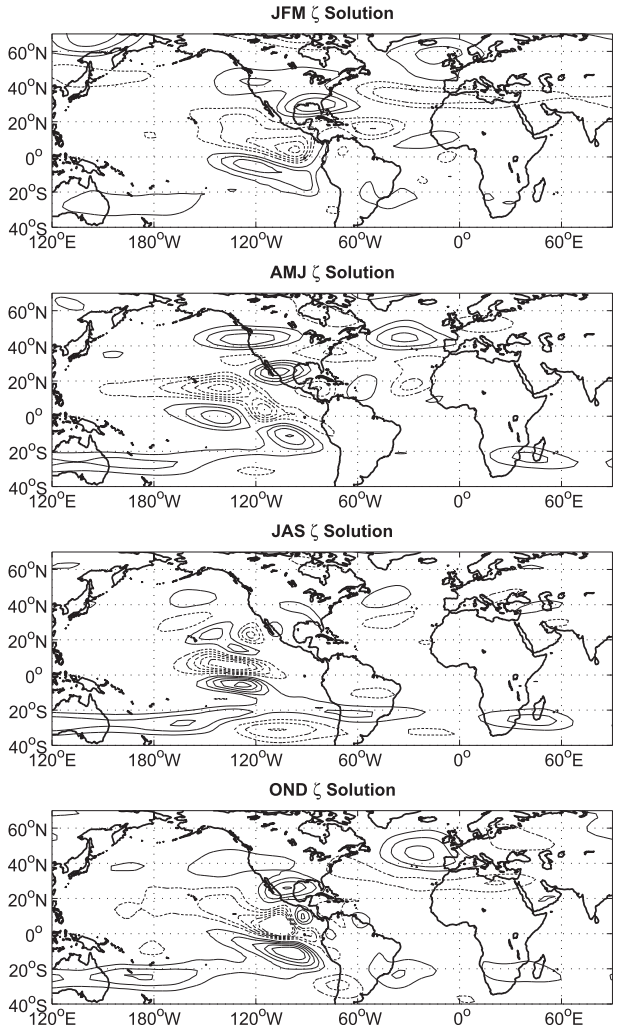

FIG. 9. As in Fig. 8, but with perturbation divergence forcing applied from 0°–10°N, 150°–90°W.

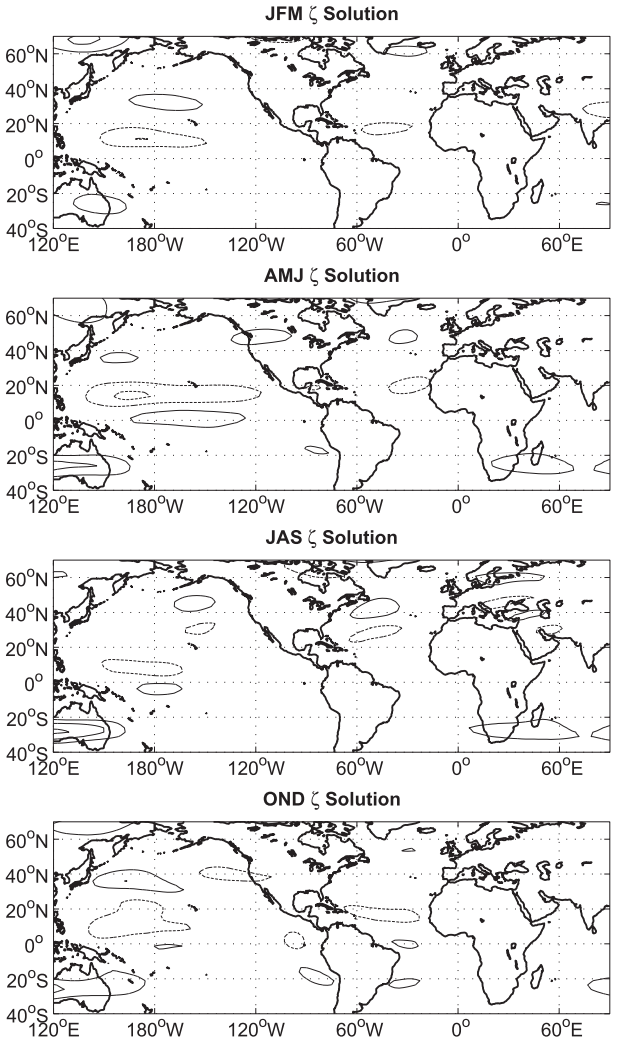

FIG. 10. As in Fig. 8, but with perturbation divergence forcing applied from 0°–10°N, 150°E–150°W.

Not only does the LBVE model not capture moist processes or baroclinic and nonlinear effects, but also, by virtue of linearization about an ''average'' background state, the model ignores transient, subseasonal variability that may be more or less conducive for Rossby wave signal propagation (Held et al. 2002).

a. Composite analysis of the long run

Seasonal ENSO-based composites of upper- and lower-tropospheric fields were derived from the 1870–1999 continuous run of the AGCM. Composites of precipitation over the Pacific were similar to observations with increased precipitation along the ITCZ north of the equator and on both sides of the equator in the central Pacific (not shown).

For the JFM season, the 200-hPa vorticity composite reveals a wave train of alternately signed anomalies that emanates from the equatorial Pacific and propagates northeastward over the central United States, whereupon the wave train refracts off the jet over North America and moves southeastward over the subtropical North Atlantic Ocean (Fig. 11). The path of this seasonal wave train has previously been described using ray tracing (Shaman and Tziperman 2005) and has been represented in composite fields from other AGCM integrations (Pohlmann and Latif 2005). This model-derived pattern of vorticity anomalies closely matches the ENSO-based composites made using NNR (Fig. 1). In both the CAM and NNR composites, the vorticity anomalies, as well as 200-hPa zonal wind anomalies, are centered over the western Atlantic and North America, well to the west of the European coast. The CAM composites also capture the strong North Pacific vorticity anomalies seen in the NNR composites. The CAM

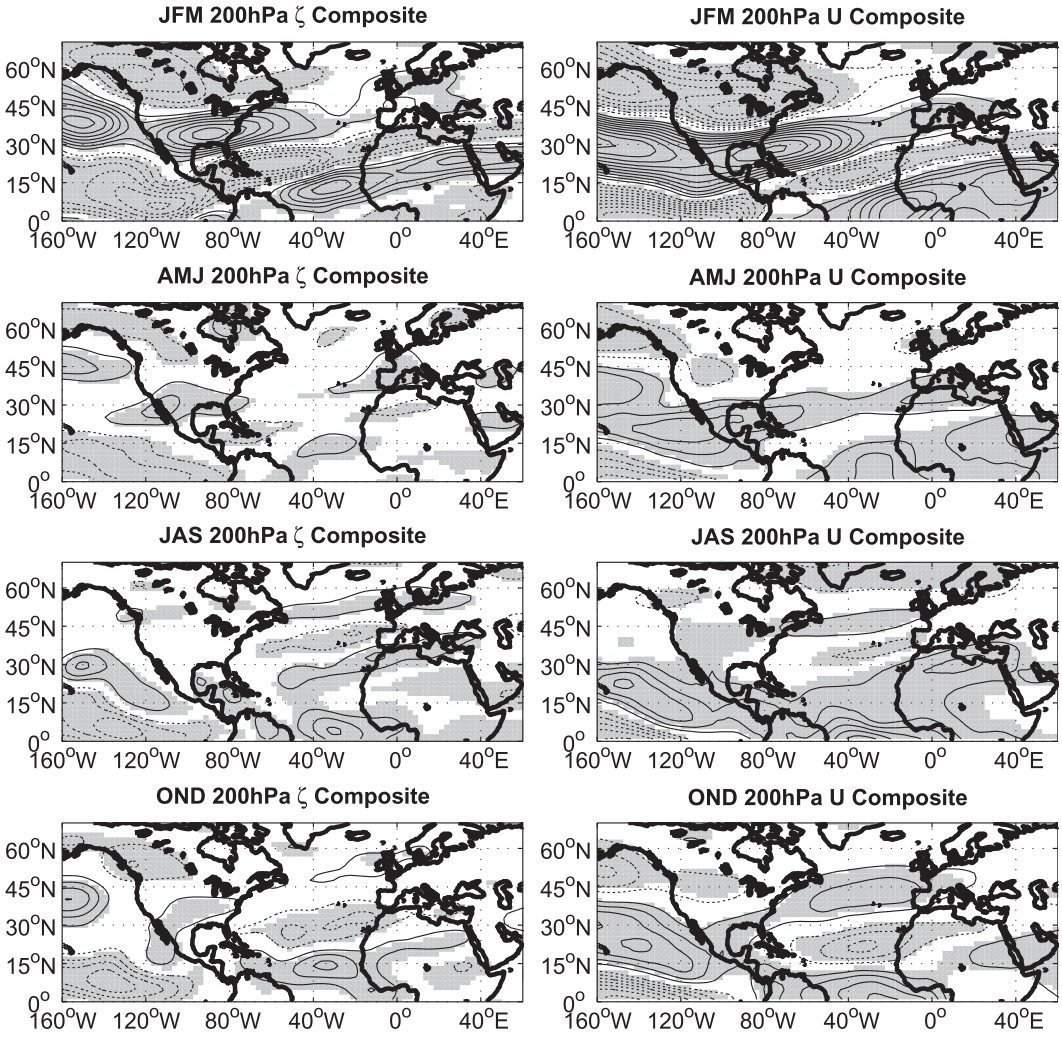

FIG. 11. The 3-month seasonal ENSO-based composites of 200-hPa (left) relative vorticity and (right) zonal wind derived from an 1870–1999 integration of CAM4. The contour intervals are (left) $4 \times 10^{-6}\,\mathrm{s}^{-1}$ and (right) $2\,\mathrm{m\,s}^{-1}$. Negative contours are dotted and the zero contour is omitted. Gray areas denote regions significant at the 95% level ($p < 0.05$) based on bootstrap confidence intervals estimated by the generation of 5000 random CAM4 composite maps for each 3-month seasonal period.

composites, however, are centered slightly to the north of the NNR.

For AMJ, the CAM composites of upper-tropospheric conditions reveal a weak ENSO response that is similar to the NNR ENSO-based composite and the forced solution of the LBVE model. Namely, both composites and the LBVE model produce a positive vorticity anomaly along the European coast centered around 45°N. The CAM long-run composite anomaly is situated farther east and to the south directly over the western European coast, whereas the LBVE model solution and NNR composite anomalies are to the west of the British Isles. Both the CAM long-run and NNR composites have a weak negative anomaly to the south of the positive anomaly, which forms a dipole that is reminiscent of the OND response, though weaker. In addition, the CAM long-run composites show weak westerly wind anomalies over southern Iberia and North Africa. These winds are stronger and shifted to the south of the NNR composite winds (Fig. 1).

For the JAS season, the CAM long-run composite produces a positive anomaly over the subtropical Atlantic, North Africa, and the Mediterranean Sea that is coincident with the NAA jet (Fig. 11). Increased winds are also evident along the southern flank of the jet. Both these features are evident in the 200-hPa NNR composites (Fig. 1). North of the NAA jet over the North Atlantic and western Europe the CAM composites

exhibit additional vorticity and wind anomalies that possess an orientation from west-southwest to east-northeast. The NNR has similarly oriented composite anomalies in both vorticity and zonal wind; however, these anomalies are farther to the north than in the AGCM.

The CAM long-run OND composite captures much of the seasonal ENSO-related 200-hPa variability over the North Atlantic from 0° to 50°N. Unlike the forced solution of the LBVE model (Fig. 3), the CAM long run depicts a north–south column of alternating vorticity and wind anomalies over the Atlantic, including a positive vorticity anomaly at 15°N, a negative vorticity anomaly at 30°N, and a positive vorticity anomaly at 50°N. A similar pattern, offset to the south, is evident in the zonal wind composite. These patterns better match the NNR composites for this season, though they fail to capture the vorticity and wind anomalies north of 60°N.

The OND CAM long-run composites, however, also show a diminution in the strength of the vorticity response over and west of Great Britain that underrepresents this feature as seen in the NNR composites. Indeed, the LBVE model solutions seem to better capture this response, which is critical for the ENSO teleconnection with Europe. These results suggest that additional processes within CAM may be overly dampening the direct Rossby wave response to ENSO variability.

Overall, the CAM long run captures many of the prominent features of seasonal upper-tropospheric ENSO-related variability over the North Atlantic and Europe. Specifically, the model simulates the seasonal changes in the magnitude of the teleconnection with a strong boreal fall and winter response but a weaker boreal spring and summer response. CAM does a much better job than the LBVE model depicting the JFM response to ENSO, including the response over the North Pacific. Clearly, inclusion of the processes absent from the LBVE model, such as transient, nonlinear, and baroclinic effects, improved representation of the wintertime response. CAM4 also includes stratospheric pressure levels; previous work has indicated that stratospheric conditions and wave activity may mediate the ENSO–European teleconnection during winter (Ineson and Scaife 2009), so a possible role for the stratosphere in modulating the wintertime Rossby wave response also exists.

The position of the upper-tropospheric ENSO-related anomalies during AMJ and OND is also better simulated with CAM than forced solutions of the LBVE model. This finding suggests that while the basis of the teleconnection is determined by a stationary barotropic Rossby wave train, downstream processes modify the seasonal atmospheric response over the North Atlantic and Europe. Indeed, in boreal winter such modification is important and alters the trajectory and magnitude of the response (including over the North Pacific), whereas in spring and fall the modifications are more limited and result in an amplification at the exit region of the North Atlantic jet and an alignment of anomalies along the European and North African coasts.

Composites of lower-tropospheric variables are next presented. The zonal wind ENSO composite structure for JFM roughly matches reanalysis, with a negative wind anomaly slanting from west-southwest to east-northeast stretching from 48°N near New Brunswick, Canada, to Scandinavia, as well as positive wind anomalies to the north and south of this negative wind anomaly (Fig. 12). However, the magnitude of these zonal wind anomalies in the CAM simulation is much less than seen in reanalysis. This reduced magnitude, in conjunction with weak inaccurate 850-hPa moisture anomalies in the sector, leads to zonal moisture advection anomalies over the North Atlantic that are much weaker than seen in reanalysis (Shaman 2013, manuscript submitted to *J. Climate*).

For the AMJ and JAS seasons, both the CAM and NNR lower-tropospheric zonal wind and zonal moisture advection composites did not produce a strong signal. For both seasons between 40° and 56°N, the easterly anomalies seen in the reanalysis composites (Fig. 4 of Shaman 2013, manuscript submitted to *J. Climate*) are shifted to the west in the CAM composites (Fig. 12), well away from the European coast and the easterly wind anomalies seen in the upper troposphere (Fig. 11). However, the CAM composites for both AMJ and JAS have westerly anomalies of both zonal wind and zonal moisture advection over the North Atlantic south of 40°N and extending to southern Europe, which is in agreement with reanalysis.

The OND CAM ENSO composite shows an 850-hPa zonal wind anomaly that roughly matches the dipole response in the upper troposphere. OND is the only season that produces the semblance of an equivalent barotropic response within the model over the North Atlantic. However, this projection to the lower troposphere is weaker than in reanalysis and shifted a bit to the west.

Overall, the CAM long-run seasonal composites depict the ENSO–upper tropospheric teleconnection over the North Atlantic and Europe, but do not represent ENSO-related variability in the lower troposphere well, particularly along the western European coast.

b. CAM perpetual-run experiments

To more clearly identify the forcing region associated with the seasonal ENSO-related response over the North Atlantic and Europe within the CAM and to determine

FIG. 12. The 3-month seasonal ENSO-based composites of 850-hPa (left) zonal wind, (center) specific humidity, and (right) zonal humidity flux derived from an 1870–1999 integration of CAM4. The contour intervals are (left) 0.5 m s^{-1}, (center) 1×10^{-4} kg kg^{-1}, and (right) 2×10^{-3} kg kg^{-1} m s^{-1}. Negative contours are dotted and the zero contour is omitted. Gray areas denote regions significant at the 95% level ($p < 0.05$) based on bootstrap confidence intervals estimated by generation of 5000 random CAM4 composite maps for each 3-month seasonal period.

whether this seasonal response was itself dependent on the seasonal cycle, a suite of forced experiments were next performed with CAM4 fixed to run perpetually on a specified date. The 20-yr perpetual simulations were run for the dates 14 February, 15 May, 15 August, and 15 November forced with either average monthly El Niño or La Niña conditions. The last 10 yr of these integrations were then used to construct El Niño minus La Niña composites of the atmospheric response.

Figure 13 presents El Niño minus La Niña composites of 200-hPa relative vorticity and zonal wind for perpetual simulations forced with global ENSO SSTs and sea ice. The upper-tropospheric response produced by these forced simulations is very similar to the seasonal composites derived from the long run of CAM (Fig. 11). Specifically, the 14 February perpetual-forced simulation composites produce the same strong wintertime teleconnection pattern centered over the western Atlantic and North America.

Of the four perpetual dates, the 15 May perpetual composite has the weakest match with its corresponding seasonal (AMJ) long-run composite, particularly over the North Atlantic and Europe. In that region, the perpetual composite fails to capture the weak positive

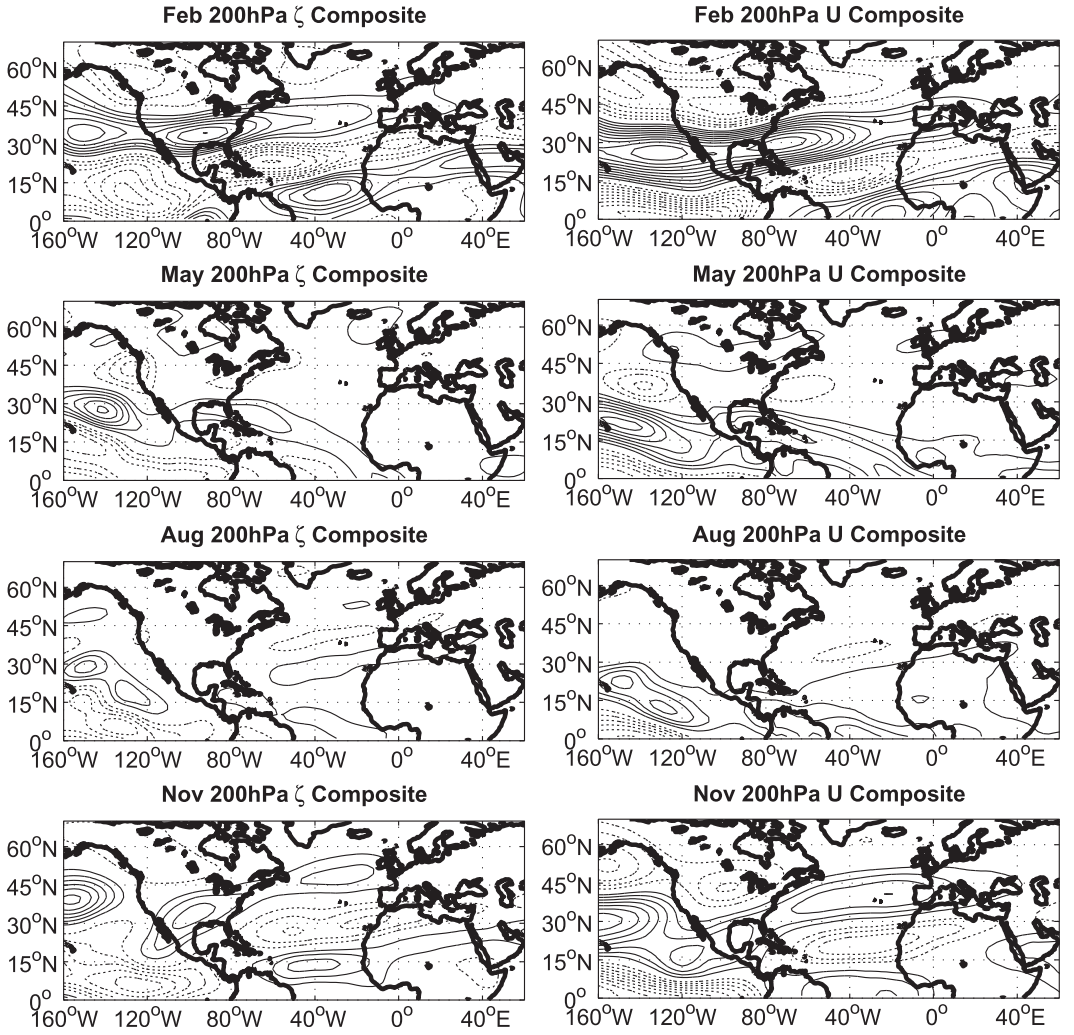

FIG. 13. El Niño minus La Niña composites of 200-hPa (left) relative vorticity and (right) zonal wind derived from years 11–20 of forced 20-yr perpetual runs of CAM4 fixed to 14 Feb, 15 May, 15 Aug, and 15 Nov. Global average El Niño and La Niña SST and sea ice conditions for the respective month of the perpetual setting were used to force these integrations. The contour intervals are (left) $4 \times 10^{-6}\,s^{-1}$ and (right) $2\,m\,s^{-1}$. Negative contours are dotted and the zero contour is omitted.

anomaly near the British Isles seen in the long-run composite (Fig. 11) and reanalysis (Fig. 1).

The perpetual 15 August upper-tropospheric composites (Fig. 13) are very similar to their long-run JAS counterpart. Over the North Atlantic, the response is primarily in the NAA jet and over open water. The 15 November perpetual composites are also similar to their long-run (OND) counterpart. The anomalous relative vorticity maxima off the west coast of Europe and Africa are stronger in the perpetual composite, which is more representative of reanalysis (Fig. 1). Strong onshore westerlies over southern Europe are also produced in the 15 November perpetual composite.

The similarity of the long-run and perpetual-run CAM composites for the winter, summer, and fall seasons indicates that ENSO-related differences in SSTs and sea ice produce a simultaneous seasonal atmospheric response over the North Atlantic and Europe within this model. That is, the response is not dependent on antecedent conditions, such as prior season SSTs or land snow cover.

Experiments were next performed to determine whether the model response over the North Atlantic and Europe is primarily because of tropical Pacific SST variability and not associated with SST or sea ice changes in other oceanic regions. Forced perpetual simulations were repeated but with average monthly El Niño or La Niña SST conditions only applied in the tropical Pacific between 30°S and 30°N. Outside the tropical Pacific, monthly climatological SSTs and sea ice were imposed.

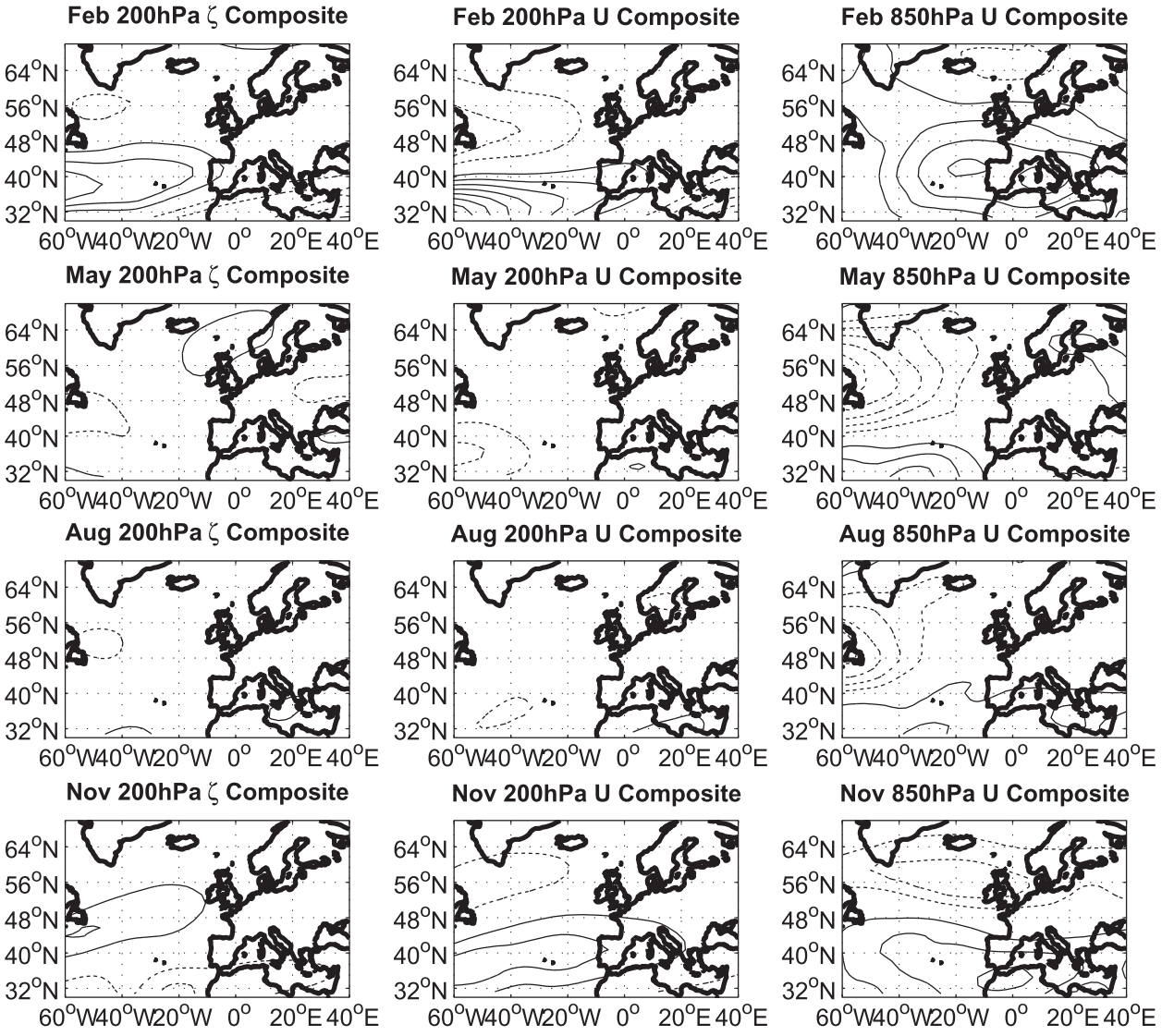

FIG. 14. El Niño minus La Niña composites of (left) 200-hPa relative vorticity, (center) 200-hPa zonal wind, and (right) 850-hPa zonal wind derived from years 11–20 of forced 20-yr perpetual runs of CAM4 fixed to 14 Feb, 15 May, 15 Aug, and 15 Nov. Monthly average El Niño and La Niña SST conditions for the Pacific Ocean between 30°S and 30°N and climatological SST and sea ice conditions elsewhere for the respective month of the perpetual setting were used to force these integrations. The contour intervals are (left) $4 \times 10^{-6}\,\mathrm{s}^{-1}$, (center) $2\,\mathrm{m\,s}^{-1}$, and (right) $0.5\,\mathrm{m\,s}^{-1}$. Negative contours are dotted and the zero contour is omitted.

The composites derived from simulations forced with only tropical Pacific SST ENSO-related variability (Fig. 14) are similar to those produced using global SST and sea ice ENSO-related variability. For the perpetual 14 February simulations, the same teleconnection pattern is apparent in the upper troposphere in both the relative vorticity and zonal wind fields. In addition, in both the tropical Pacific and globally forced composites lower-tropospheric onshore wind anomalies are generated over much of western Europe, and offshore anomalies are produced along the coast of Scandinavia. These lower-tropospheric composite anomalies, which are well offset to the north and east of the upper-tropospheric zonal wind anomalies, are not present in reanalysis composites (Fig. 4 of Shaman 2013, manuscript submitted to *J. Climate*); rather, reanalysis depicts an equivalent barotropic structure in the zonal wind composites during JFM.

The 15 May and 15 August composites derived from the tropically forced perpetual simulations reveal only a nominal upper-tropospheric response over the North Atlantic and Europe (Fig. 14). These upper-tropospheric responses are similar to the globally forced perpetual

simulation composites but more muted. The 15 May perpetual simulation composites remain dissimilar from the long-run AMJ composite (Fig. 11), which is better matched with reanalysis. On the other hand, in the lower troposphere, the 15 May and 15 August 850-hPa zonal wind perpetual-run composites are similar to the long-run composites for AMJ and JAS. None of these CAM 850-hPa zonal wind composites represent the anomalies evident in reanalysis along the European coast, though it should be noted that these reanalysis composite anomalies are for the most part not statistically significant.

The 15 November, tropically forced perpetual simulation composites are well matched with their globally forced counterparts, though the positive vorticity anomaly in the upper troposphere is centered farther west. The wind composite anomalies in both the upper and lower troposphere move onshore over southern Europe and, in the lower troposphere, are offshore over northern Europe. In this respect, all the boreal fall CAM simulation composites match the reanalysis.

Overall, the perpetual simulations reveal that the bulk of the upper-tropospheric response over the North Atlantic and Europe during the fall and winter is forced by variability in the tropical Pacific and that this response is relatively instantaneous. Certainly, there is some role for forcing from other regions and antecedent conditions, as demonstrated by prior studies. For instance, Mathieu et al. (2004) found that Atlantic SSTs have a role determining the North Atlantic–European response to individual El Niño events using the Hadley Centre AGCM. However, as represented by CAM4, these effects are less predominant than the seasonally instantaneous, tropical Pacific–forced response.

Both the perpetual and long-run CAM simulations fail to project this upper-tropospheric response appropriately to the lower troposphere during boreal winter (Figs. 13 and 14). Instead, the wintertime lower-tropospheric ENSO composite structure mimics the autumn pattern. The autumn lower-tropospheric response matches reanalysis, and through the entire troposphere, the CAM simulations produce the appropriate equivalent barotropic structure (not shown).

During boreal spring and summer, the North Atlantic and European response within CAM to ENSO-related forcing is much more muted. Some features seen in reanalysis are reproduced, in particular the NAA jet response during summer. Other features around the British Isles, such as the offshore winds during summer, are not represented; however, these latter composite reanalysis features are for the most part not statistically significant and do not offer a robust target for model comparison.

5. LBVE with CAM fields

The long-run and perpetual CAM 200-hPa climatological fields were next used as the background for further forced simulations with the LBVE model. Divergence forcing set to $3 \times 10^{-6}\,s^{-1}$, as used in all other LBVE experiments, was imposed at 0°–10°N, 170°–270°E on the steady-state LBVE model [Eq. (2.1)]. These simulations were used to determine if fundamental differences between the CAM-simulated and NNR basic state might account for the changes in upper-tropospheric response to ENSO-related variability seen among simulations with the LBVE model (Fig. 3) and CAM (Figs. 11, 13, and 14).

The results using the monthly long-run CAM climatologies as the background produced results (Fig. 15) consistent with the forced solutions found using reanalysis as the climatology (Fig. 3). This finding indicates that the pronounced difference in the CAM long-run composites, particularly in boreal winter when the AGCM better captures the ENSO-related variability seen in reanalysis composites, is principally because of processes represented in the AGCM that are absent from the LBVE model and is not because of a discrepancy between the CAM and NNR mean fields.

The LBVE model solutions made using the perpetual CAM climatologies as the background are similar to the long-run and reanalysis solutions for boreal winter and summer backgrounds. The perpetual February background produces a weaker LBVE-forced response over the North Atlantic than the long-run February climatology, but in similar fashion fails to produce the strong recurving wave train pattern over North America and the western North Atlantic (e.g., Fig. 11). The perpetual August background produces little response over the North Atlantic, except in the NAA jet, as is seen for the same forcing of the CAM long-run and reanalysis boreal summer climatology backgrounds with the LBVE model. The perpetual November background yields a stronger North Atlantic response than either the CAM long-run or reanalysis backgrounds; however, the form of the response is similar (Fig. 15).

Only forcing of the May perpetual background produces a steady-state LBVE model solution that is distinct in pattern from other boreal spring solutions. Similarly, the perpetual May CAM composites (Fig. 14) were dissimilar to their long-run AMJ CAM composite counterparts (Fig. 11). To determine if large discrepancies in the seasonal-mean state existed among CAM and NNR, additional perpetual date simulations were performed with CAM but using 1949–2011 climatological SST forcing. This investigation revealed that the perpetual May 200-hPa zonal wind mean field, as forced

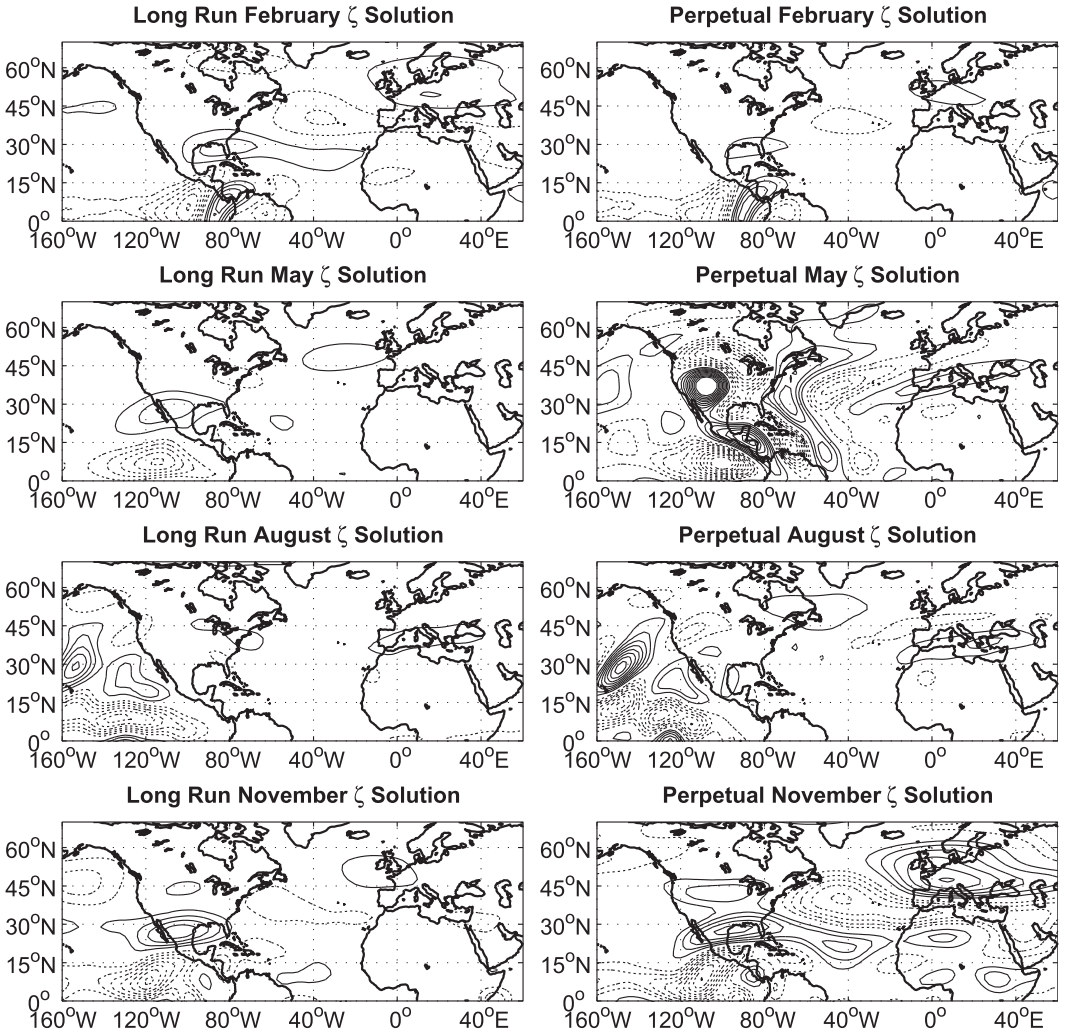

FIG. 15. Vorticity solution of steady-state LBVE model linearized about CAM (left) long-run and (right) perpetual-run monthly 200-hPa climatologies and forced with perturbation divergence from 0°–10°N, 170°E–90°W. The contour interval is $4 \times 10^{-6}\,s^{-1}$. Negative contours are dashed and the zero contour is omitted.

with climatological SSTs, differed substantially from NNR climatology, whereas the long-run May climatology did not (Fig. 16). Perpetual runs with alternate spring dates (e.g., 1 June) had similar discrepancies in the mean upper-tropospheric winds. This problem did not afflict other seasons (not shown). Thus, it appears that while other seasons were fine, the perpetual runs during boreal spring did not produce a realistic upper-tropospheric climatology. Consequently, the 15 May perpetual-run ENSO-forced composites shown in Figs. 13 and 14 should be interpreted with caution.

6. Discussion

The model experiments presented here indicate that ENSO-associated upper-tropospheric vorticity anomalies over the North Atlantic and Europe are principally produced by Rossby waves that manifest in the upper troposphere and that atmospheric interactions and feedback with those Rossby waves alters the spatial structure and amplitude of the response, particularly during the JFM season. This teleconnection is evident, in its most basic form, during boreal fall, winter, and spring as an eastward-propagating stationary barotropic Rossby wave train. These waves are excited primarily by forcing over the far eastern equatorial Pacific. The wave train appears to amplify in the vicinity of the British Isles, producing a stronger anomaly in this region, which is coincident with the exit of the North Atlantic jet. Simulation of this basic wave train response is produced by the LBVE model with divergence forcing.

Simulations with both the full Rossby wave source LBVE model and CAM4 indicate that other processes,

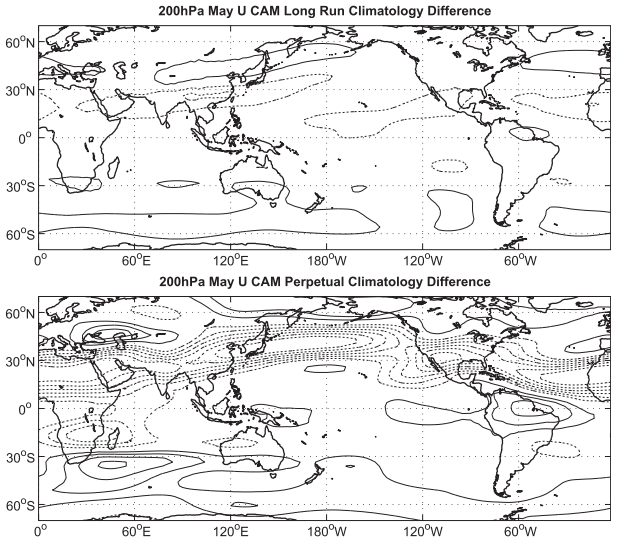

FIG. 16. May CAM (top) long-run and (bottom) perpetual-run 200-hPa zonal wind climatologies with May 1949–2011 NNR 200-hPa climatological zonal wind subtracted. The contour interval is 5 m s^{-1}. Negative contours are dashed and the zero contour is omitted.

including vorticity advection, modify and attenuate the basic wave train response. During boreal winter the Rossby wave train path is greatly affected by downstream processes and instead appears to reflect off the jet over North America and propagate to the southeast over the Atlantic Ocean. During boreal spring, the response at the North Atlantic jet exit is weakened in AGCM simulations. The jet exit response remains the most robust during boreal fall. These simulations are consistent with observational findings (Shaman 2013, manuscript submitted to *J. Climate*).

The sensitivity of the North Atlantic upper-tropospheric vorticity response to the forcing location is apparent in the LBVE model experiments. Forcing over the far eastern tropical Pacific is needed to excite the eastward-propagating wave trains during boreal fall, winter, and spring. This finding suggests that the North Atlantic/European sector response will depend on the structure of the ENSO event. For instance, El Niño Modoki events (characterized by warming in the central tropical Pacific but not the eastern tropical Pacific) should not affect conditions over the North Atlantic as strongly as a canonical El Niño event. Similarly, Toniazzo and Scaife (2006) noted that the observed wintertime ENSO–European teleconnection developed more fully during strong El Niño events characterized by larger SST anomalies and greater precipitation in the eastern Pacific. Indeed, the findings indicate that divergence forcing over the far eastern Pacific is crucial for producing the responses seen in reanalysis composites during boreal fall, winter, and spring.

In addition, the wave train response appears to depend critically on seasonal wind patterns. During boreal summer, easterlies over the tropical Pacific (Fig. 4) are associated with a change in the character of the teleconnection that includes both eastward- and westward-propagating signals and a relatively weak upper-tropospheric response over western Europe. Rossby wave propagation out of the tropics is typically reduced by tropical easterlies (Li and Nathan 1997). Here, the summer easterlies may limit the strong northeastward upper-tropospheric Rossby wave propagation needed to produce significant anomalies over the North Atlantic and coastal Europe. In addition, the boreal summer background supports westward-propagating waves, as has previously been reported (Shaman and Tziperman 2007; Shaman et al. 2009), which interfere with the eastward-propagating signal over the North Atlantic.

In all seasons but summer, the LBVE model produces a dipole response along the European coast in response to El Niño forcing (e.g., Fig. 3). Prior work has suggested that dipole structures at jet exit regions may manifest because of instability growth processes (Simmons et al. 1983; Branstator 1985). In particular, Li and Nathan (1997) showed that energy conversion can produce unstable modes at jet exits where eddy momentum fluxes are concentrated. However, the LBVE model captures much of the dipole signal while not representing many atmospheric processes, including transient activity and nonlinear feedbacks. This finding indicates that simple forcing of the flow is a principal determinant of the dipole response off the European coast. Similar relationships between tropical forcing and jet exit response have been suggested from observational analysis (Blackmon et al. 1984) and supported by modeling studies (Held et al. 1989; Hoerling and Ting 1994). While feedback from eddy momentum fluxes may still reinforce or alter the jet exit region anomaly response pattern, such as seen during JFM, the LBVE model experiments indicate that the direct response of the mean flow itself to tropical forcing can be large (Ting and Held 1990; Held et al. 2002), such as seen during the AMJ and OND seasons here. Still, the role that feedback may play in maintaining and reinforcing the observed jet exit response needs to be studied further.

The primary focus of this study is the investigation of the mechanisms underpinning the teleconnection between the tropical Pacific and the North Atlantic/European sector in the upper troposphere as simulated by a hierarchy of model forms; however, some consideration of the simulated lower-tropospheric response is warranted. In observations, the European coastal upper-tropospheric anomalies project to the surface and produce onshore moisture advection near the surface (Shaman

2013, manuscript submitted to *J. Climate*). However, in the AGCM simulations presented here, these lower-tropospheric responses are not well captured. Specifically, during winter the 850-hPa zonal wind response is too far to the east, and in the other seasons, particularly spring and summer, it is often too far west (Figs. 12 and 14). So while the large-scale upper-tropospheric response to ENSO over the North Atlantic is often well simulated, the attendant lower-tropospheric response is not. These inaccuracies would affect ENSO-related precipitation anomaly rates within the AGCM. Such deficiencies need to be explored further.

Future work should also test the effect of model resolution on the findings, as the wintertime North Atlantic/European response to ENSO may be better represented in a high-resolution model setting (Merkel and Latif 2002). Higher resolution may be particularly important for resolving smaller-scale features in the lower troposphere. In addition, this work has explored the average response to ENSO events without consideration of decadal-scale variability. Future study should explore the effects of downstream systems, such as the Pacific decadal oscillation and the North Atlantic Oscillation (Zanchettin et al. 2008), as well as volcanic activity and stratospheric conditions (Brönnimann 2007; Ineson and Scaife 2009), all of which could modulate the described Rossby wave teleconnection linking ENSO with the North Atlantic and Europe.

Overall, the models replicate the stronger boreal fall and winter response and the weaker spring and summer response seen in the reanalysis composites. Furthermore, the AGCM perpetual simulations indicate that these seasonal teleconnections do not rely strongly on prior conditions; rather, the upper-tropospheric responses to ENSO in the North Atlantic/European sector are seasonally instantaneous. In general, much of the seasonal teleconnection between ENSO and variability over the North Atlantic and Europe seems to be mediated by Rossby wave communication through the atmosphere.

Acknowledgments. I thank Eli Tziperman for helpful discussions. This work was supported by NSF Climate and Large-Scale Dynamics Grant AGS-1205043.

REFERENCES

Adler, R. F., and Coauthors, 2003: The version-2 Global Precipitation Climatology Project (GPCP) monthly precipitation analysis (1979–present). *J. Hydrometeor.,* **4,** 1147–1167.

Blackmon, M. L., Y.-H. Lee, J. M. Wallace, and H.-H. Hsu, 1984: Time variation of 500 mb height fluctuations with long, intermediate and short time scales as deduced from lag-correlation statistics. *J. Atmos. Sci.,* **41,** 981–991.

Branstator, G., 1983: Horizontal energy propagation in a barotropic atmosphere with meridional and zonal structure. *J. Atmos. Sci.,* **40,** 1689–1708.

——, 1985: Analysis of general circulation model sea-surface temperature anomaly simulations using a linear model. Part II: Eigenanalysis. *J. Atmos. Sci.,* **42,** 2242–2254.

Brönnimann, S., 2007: Impact of El Niño–Southern Oscillation on European climate. *Rev. Geophys.,* **45,** RG3003, doi:10.1029/2006RG000199.

Dong, B. W., R. T. Sutton, S. P. Jewson, A. O'Neill, and J. M. Slingo, 2000: Predictable winter climate in the North Atlantic sector during the 1997–1999 ENSO cycle. *Geophys. Res. Lett.,* **27,** 985–988.

Feddersen, H., 2003: Predictability of seasonal precipitation in the Nordic region. *Tellus,* **55A,** 385–400.

Greatbatch, R. J., and T. Jung, 2007: Local versus tropical diabatic heating and the winter North Atlantic Oscillation. *J. Climate,* **20,** 2058–2075.

——, J. Lu, and K. A. Peterson, 2004: Nonstationary impact of ENSO on Euro-Atlantic winter climate. *Geophys. Res. Lett.,* **31,** L02208, doi:10.1029/2003GL018542.

Grötzner, A., M. Latif, and D. Dommenget, 2000: Atmospheric response to sea surface temperature anomalies during El Niño 1997/98 as simulated by ECHAM4. *Quart. J. Roy. Meteor. Soc.,* **126,** 2175–2198.

Held, I. M., S. W. Lyons, and S. Nigam, 1989: Transients and the extratropical response to El Niño. *J. Atmos. Sci.,* **46,** 163–174.

——, M.-F. Ting, and H. L. Wang, 2002: Northern winter stationary waves: Theory and modeling. *J. Climate,* **15,** 2125–2144.

Hoerling, M. P., and M.-F. Ting, 1994: Organization of extratropical transients during El Niño. *J. Climate,* **7,** 745–766.

Hoskins, B. J., and K. Karoly, 1981: The steady response of a spherical atmosphere to thermal and orographic forcing. *J. Atmos. Sci.,* **38,** 1179–1196.

Hurrell, J. W., J. J. Hack, D. Shea, J. M. Caron, and J. Rosinski, 2008: A new sea surface temperature and sea ice boundary dataset for the Community Atmosphere Model. *J. Climate,* **21,** 5145–5153.

Ineson, S., and A. Scaife, 2009: The role of the stratosphere in the European climate response to El Niño. *Nat. Geosci.,* **2,** 32–36.

Janowiak, J. E., and P. Xie, 1999: CAMS–OPI: A global satellite–rain gauge merged product for real-time precipitation monitoring applications. *J. Climate,* **12,** 3335–3342.

Kalnay, E., and Coauthors, 1996: The NCEP/NCAR 40-Year Reanalysis Project. *Bull. Amer. Meteor. Soc.,* **77,** 437–471.

Li, Z., and T. R. Nathan, 1997: Effects of low-frequency tropical forcing on intraseasonal tropical-extratropical interactions. *J. Atmos. Sci.,* **54,** 332–346.

Mathieu, P.-P., R. T. Sutton, B. Dong, and M. Collins, 2004: Predictability of winter climate over the North Atlantic European region during ENSO events. *J. Climate,* **17,** 1953–1974.

Merkel, U., and M. Latif, 2002: A high resolution AGCM study of the El Niño impact on the North Atlantic/European sector. *Geophys. Res. Lett.,* **29** (9), doi:10.1029/2001GL013726.

Neale, R. B., and Coauthors, 2010: Description of the NCAR Community Climate Model (CAM 4.0). NCAR Tech. Note TN-485+STR, 224 pp.

Park, S., 2004: Remote ENSO influence on Mediterranean sky conditions during late summer and autumn: Evidence for a slowly evolving atmospheric bridge. *Quart. J. Roy. Meteor. Soc.,* **130,** 2409–2422.

Pohlmann, H., and M. Latif, 2005: Atlantic versus Indo-Pacific influence on Atlantic-European climate. *Geophys. Res. Lett.,* **32,** L05707, doi:10.1029/2004GL021316.

Sardeshmukh, P. D., and B. J. Hoskins, 1988: The generation of global rotational flow by steady idealized tropical divergence. *J. Atmos. Sci.,* **45,** 1228–1251.

Shaman, J., and E. Tziperman, 2005: The effect of ENSO on Tibetan Plateau snow depth: A stationary wave teleconnection mechanism and implications for the South Asian monsoons. *J. Climate,* **18,** 2067–2079.

——, and ——, 2007: The summertime ENSO–North African–Asian jet teleconnection and implications for the Indian monsoons. *Geophys. Res. Lett.,* **34,** L11702, doi:10.1029/2006GL029143.

——, and ——, 2011: An atmospheric teleconnection linking ENSO and southwestern European precipitation. *J. Climate,* **24,** 124–139.

——, S. K. Esbensen, and E. D. Maloney, 2009: The dynamics of the ENSO–Atlantic hurricane teleconnection: ENSO-related changes to the North African–Asian jet affect Atlantic basin tropical cyclogenesis. *J. Climate,* **22,** 2458–2482.

Simmons, A. J., J. M. Wallace, and G. W. Branstator, 1983: Barotropic wave propagation and instability, and atmospheric teleconnection patterns. *J. Atmos. Sci.,* **40,** 1363–1392.

Ting, M.-F., and I. M. Held, 1990: The stationary wave response to a tropical SST anomaly in an idealized GCM. *J. Atmos. Sci.,* **47,** 2546–2566.

Toniazzo, T., and A. A. Scaife, 2006: The influence of ENSO on winter North Atlantic climate. *Geophys. Res. Lett.,* **33,** L24704, doi:10.1029/2006GL027881.

Xie, P. P., and P. A. Arkin, 1997: Global precipitation: A 17-year monthly analysis based on gauge observations, satellite estimates, and numerical model outputs. *Bull. Amer. Meteor. Soc.,* **78,** 2539–2558.

Zanchettin, D., S. W. Franks, P. Traverso, and M. Tomasino, 2008: On ENSO impacts on European wintertime rainfalls and their modulation by the NAO and the Pacific multi-decadal variability described through the PDO index. *Int. J. Climatol.,* **28,** 995–1006.